Supplement of Atmos. Meas. Tech., 13, 1467–1484, 2020
https://doi.org/10.5194/amt-13-1467-2020-supplement

Atmospheric Measurement Techniques
Open Access
EGU

Supplement of

Testing the near-field Gaussian plume inversion flux quantification technique using unmanned aerial vehicle sampling

Adil Shah et al.

Correspondence to: Adil Shah (adil.shah@manchester.ac.uk)

S1. Variability in cell pressure and temperature
S2. Water correction
S3. Calibration factors
S4. Linearity
S5. Flight survey details
S6. Controlled release details and corresponding UAV aerial flight tracks
S7. Wind profiles and uncertainties
S8. Testing flux results
S9. Measurement uncertainty components
S10. Cell temperature and cell pressure during sampling

S1 Variability in cell pressure and temperature

During the MGGA Allan variance test (17 hours and 23 minutes of continuous sampling), both cell temperature and cell pressure were recorded and are plotted in Figure S1 and Figure S2, respectively, against [*X*]. Both parameters were poorly correlated, though these parameters would require further independent testing to better characterise any potential effects on [*X*]. The linear gradient between [*X*] (in ppm) and cell temperature was -0.0022 ppm ° C^{-1}, with a mole fraction zero intercept of 2.1734 ppm. The linear gradient between [*X*] (in ppm) and cell pressure was -0.0022 ppm $mbar^{-1}$, with a mole fraction zero intercept of 4.3014 ppm.

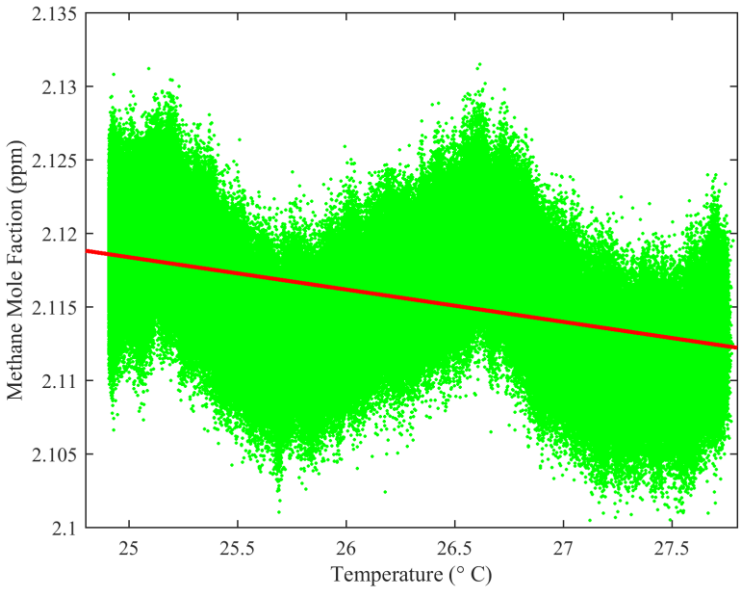

Figure S1. Variation in methane mole fraction with MGGA cell temperature (green dots), with a linear fit plotted as a red line, from 17 hours and 23 minutes of continuous sampling.

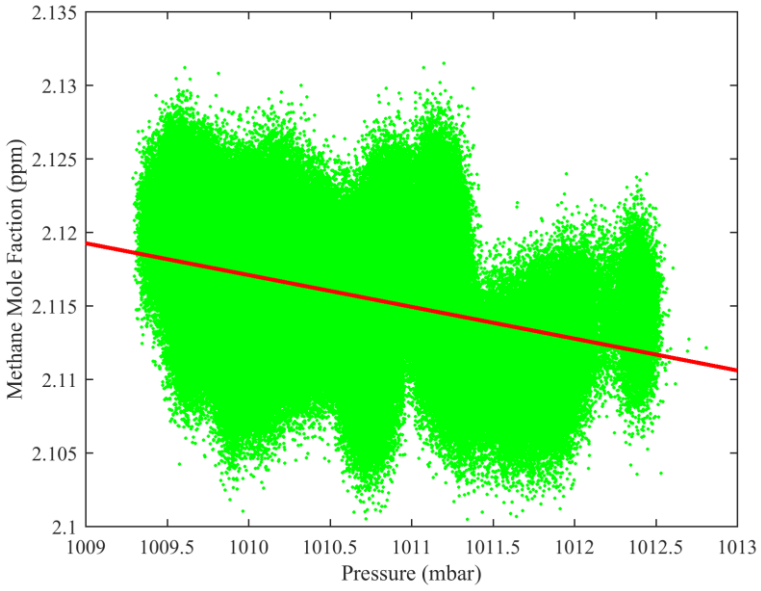

Figure S2. Variation in methane mole fraction with MGGA cell pressure (green dots), with a linear fit plotted as a red line, from 17 hours and 23 minutes of continuous sampling.

S2 Water correction

$[H_2O]_0$ was required for both instruments, in order to derive v. $[H_2O]_0$ could be modelled using Eq. (1), by fitting $[X]_0^{dry}$ to $[H_2O]_0$. This was achieved by sampling standards from three (for the MGGA) or two (for the pMGGA) gas cylinders. The precise methane content of each cylinder was not important, as this was an empirical test, characterising instrument response. The measured (black crosses) and fitted (red line) $[H_2O]_0$ values as a function of $[X]_0^{dry}$ for the MGGA and pMGGA are given in Figure S3 and Figure S4, respectively. The standard deviation $[H_2O]_0$ range for each sampled gas cylinder is also shown in Figure S3 and Figure S4.

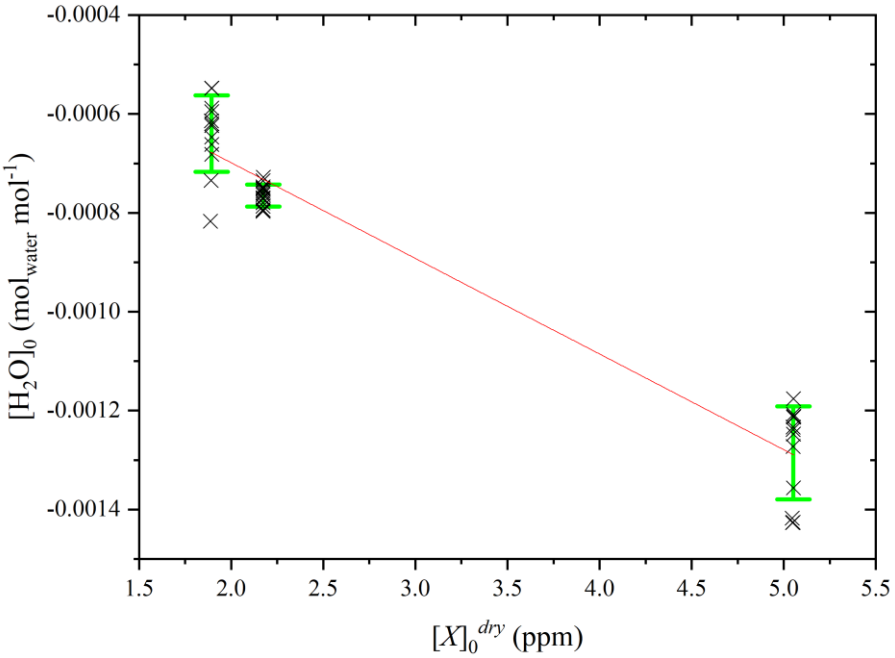

Figure S3. Measured water mole fraction offset as a function of $[X]_0^{dry}$ (black crosses) with a corresponding linear fit (red line) for the MGGA. The standard deviation water mole fraction offset range for each sampled gas cylinder is shown as a green bar.

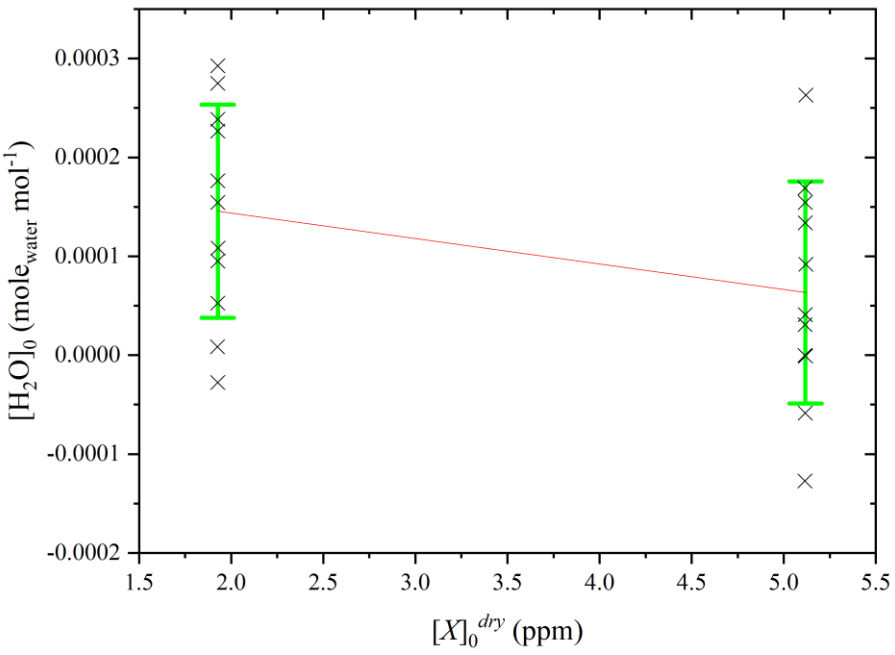

Figure S4. Measured water mole fraction offset as a function of $[X]_0^{dry}$ (black crosses) with a corresponding linear fit (red line) for the pMGGA. The standard deviation water mole fraction offset range for each sampled gas cylinder is shown as a green bar.

The temporal stability of $[H_2O]_0$ in both the MGGA and the pMGGA also assessed by performing an Allan variance precision test using a single dry air standard. The MGGA used 17 hours and 23 minutes of continuous uninterrupted sampling, while the pMGGA used 38 hours and 30 minutes of continuous uninterrupted sampling. An Allan variance was calculated for both $[H_2O]_0$ data sets, as a function of integration time. The water baseline Allan variance plot for the MGGA and pMGGA is given in Figure S5 and Figure S6, respectively.

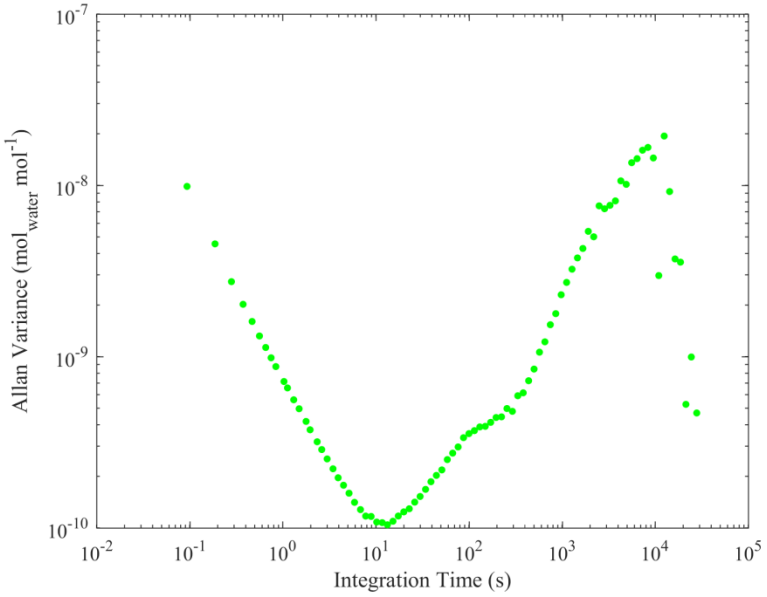

Figure S5. Allan variance of dry water mole fraction baseline for the MGGA plotted against integration time on logarithmic axes.

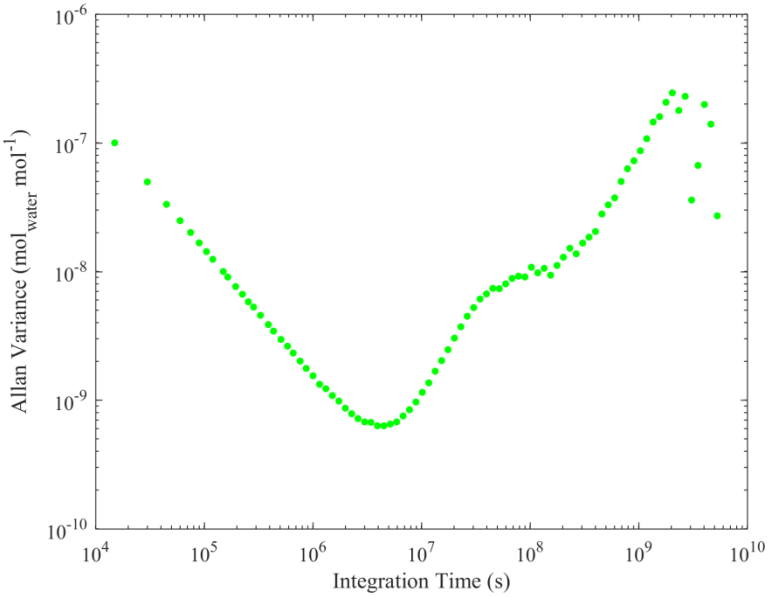

Figure S6. Allan variance of dry water mole fraction baseline for the pMGGA plotted against integration time on logarithmic axes.

Although the Allan variance precision test can be used to characterise stability, it assumes constant environmental conditions. However if one pays close attention to Figure S3 for the MGGA, it appears that the 2.2 ppm cylinder results in a water baseline below the linear fit, whereas the 1.9 ppm and 5.1 ppm cylinders result in water baseline above the linear fit. This is expected to be due to the different instrumental environmental conditions when sampling different cylinders. The 2.2 ppm cylinder was sampled at an average cell temperature of (29.48±0.04)° C and cell pressure of (1015.31±0.03) mbar. The 1.9 ppm cylinder and 5.1 ppm cylinder were sampled at an average cell temperature of (31.39±0.70)° C and cell pressure of (1005.89±0.18) mbar. A 9.4 mbar cell pressure increase and the 1.9° C cell temperature decrease may have had a cumulative effect of reducing $[H_2O]_0$ very slightly for the 2.2 ppm cylinder. These systematic temperature and pressure effects on $[H_2O]_0$ should be comprehensively characterised in future work for maximal instrumental accuracy, where a more varied range of ambient conditions is sampled. Yet as UAV sampling took place in conditions that were similar to these laboratory tests (see Table 5), the water baseline tests conducted here were sufficient.

An inherent assumption of deriving of *a* and *b* using the linear fits show in Figure S3 and Figure S4 is that $[H_2O]_0$ responds linearly up to 5 ppm (representing the maximum extent of the WMO-X2004A scale). Yet it is difficult to rule out the possibility of non-linear behaviour using only two or three data points. To comprehensively characterise linearity in the water baseline, we suggest that further could testing be conducted in future by sampling more WMO-X2004A methane mole fraction standards. As the observed change in water baseline from 1.9 ppm to 5.1 ppm is small, this is a very small component of the overall uncertainty, considering the magnitude of UAV NGI flux uncertainty ranges. For example, for the MGGA, if sampling $[X]_0^{dry}$ of 2 ppm in dry conditions (*i.e.* where ($[H_2O]$ - $[H_2O]_0$) equals zero), *v* would typically be 1. However if erroneously using the average baseline measured at $[X]_0^{dry}$ of 5.1 ppm (representing the maximum uncertainty from Figure S3 due to non-linearity), *v* would become 0.9991. This would systematically reduce a 2 ppm measurement to 1.998 ppm, representing a negligible decrease compared to other uncertainties in Eq. (11). Thus we are confident that regardless of our choice of water baseline fit, the assumption of linearity if sufficient as the baseline has little overall impact on resulting mole fraction.

Although the instruments are only calibrated up to 5 ppm (thus making any testing of $[H_2O]_0$ at a higher $[X]_0^{dry}$ not very useful) we observed $[H_2O]_0$ to increase non-linearly in the MGGA when sampling a gas standard with $[X]_0^{dry}$ of approximately 100 ppm. Plotted alongside the data in Figure S3, this can be used to produce a different linear fit (red line in Figure S7), with *a* of -0.000748 mol_{water} mol^{-1} and *b* of -0.000046 mol_{water} mol^{-1} ppm^{-1}. While these values differ from those in Table 2, these different $[H_2O]_0$ coefficients (on average) increase MGGA [*X*] measurements made during UAV1 sampling by 0.02%±0.03%.

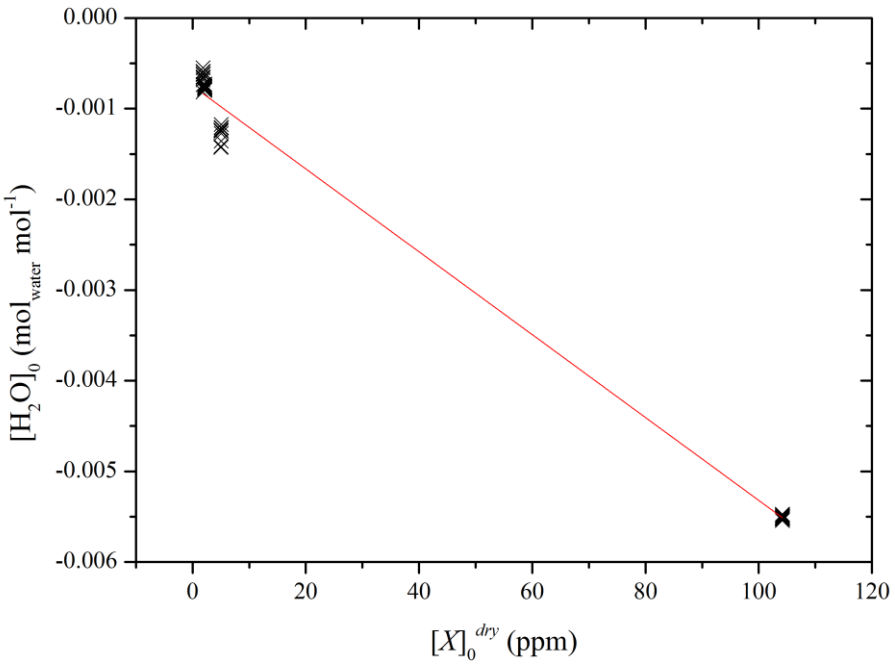

Figure S7. Measured water mole fraction offset as a function of $[X]_0^{dry}$ (black crosses) with a corresponding linear fit (red line) for the MGGA, where sampling of $[X]_0^{dry}$ of approximately 100 ppm has been included.

Each empirical water correction factor, as a function of $[H_2O]$, was calculated by sampling a humidified gas which was either dried or fed directly into the MGGA or pMGGA without drying it. An example of $[X]_0$ during the transition between dry to wet sample gas, used to derive a *v* point, in shown in Figure S8. After the humidity of the air was adjusted, the gas was sampled dry for 5 minutes, from which measurements from the final 4 minutes were taken. The gas was then sampled wet for 8 minutes, from which measurements from the final 2 minutes were taken. The gas was then sampled dry for five minutes to ensure that $[X]_0$ returned to its original dry value.

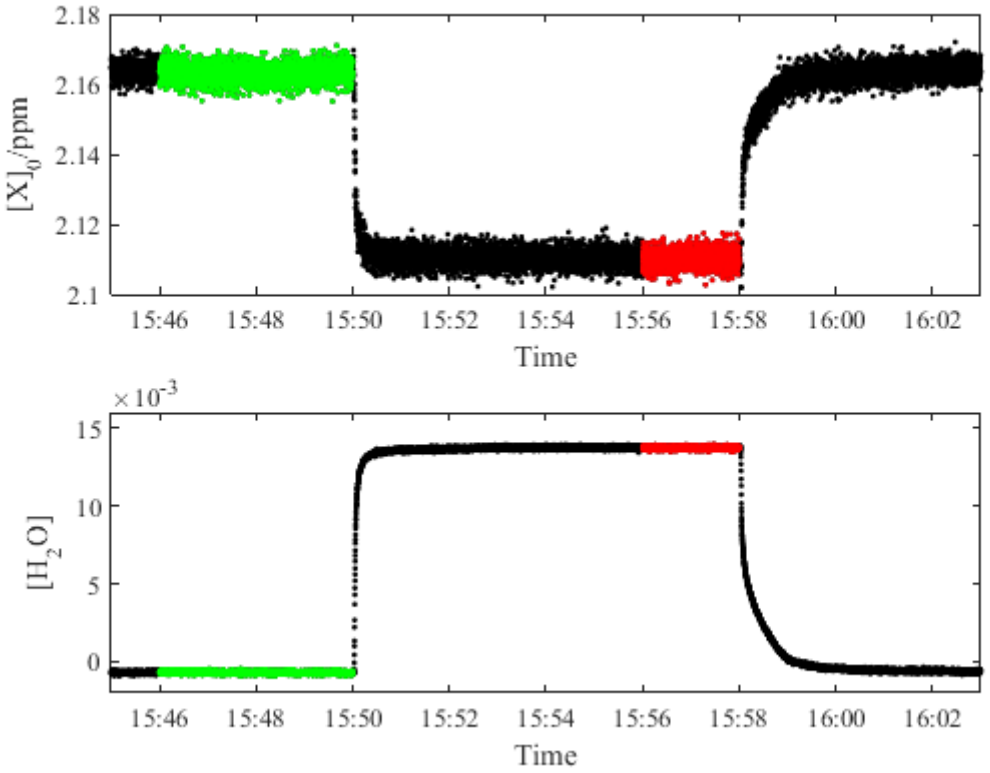

Figure S8. Uncalibrated methane mole fraction measurements (upper panel) and corresponding water mole fraction measurements (lower panel) made by the MGGA when transitioning between dry and wet gas at a dew point of 16° C. Red dots indicate measurements used to calculate $[X]_0$ and green dots indicate measurements used to calculate $[X]_0^{dry}$.

The water correction factor was plotted as a function of $[H_2O]$, corrected by the water offset, for the MGGA and pMGGA in Figure S9 and Figure S10, respectively. The data was fitted to Eq. (2) to derive the water correction parameters in Table 2. The residuals from the fit were used to derive σ_v, for each instrument. These procedures were conducted under ambient (but not controlled) cell temperature and cell pressure conditions. To better characterise the potential systematic impact of these effects in future, it may be advisable to repeat these water correction procedures in a controlled environment.

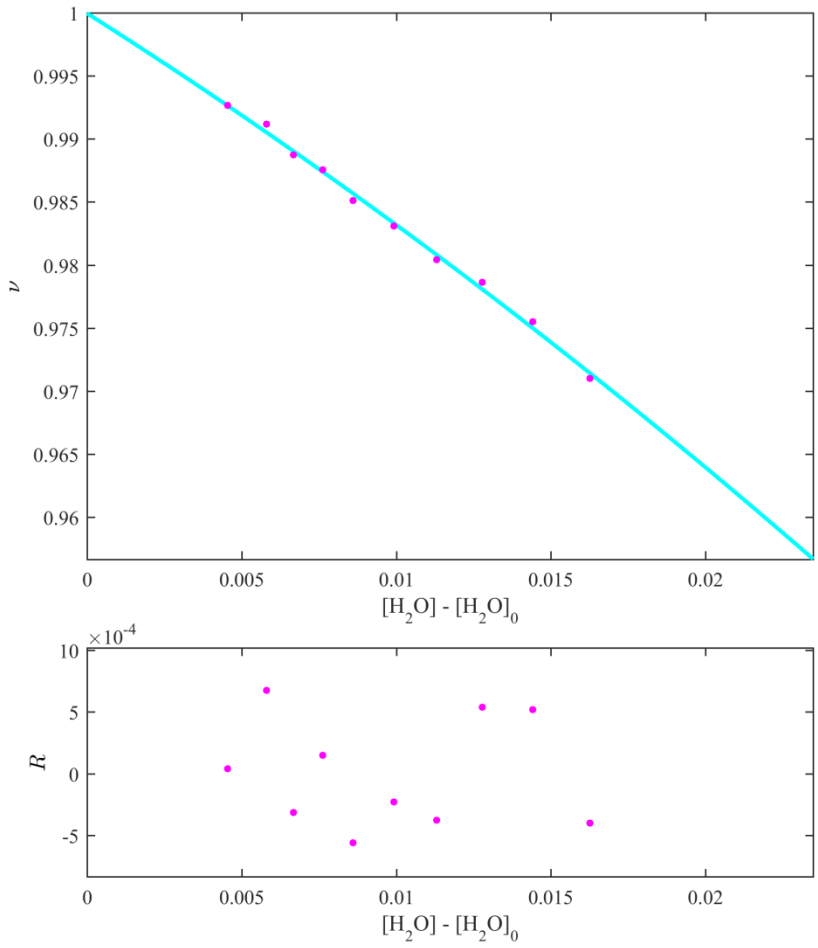

Figure S9. The empirical water correction factor (upper panel) plotted as a function of baseline corrected water mole fraction (magenta dots) for the MGGA. The cyan line is a second order polynomial fit to the data, given by Eq. (2). ν **is** $[X]_0$ **divided by** $[X]_0^{dry}$**, measured by the instrument. Corresponding residuals are given (lower panel) as magenta dots.**

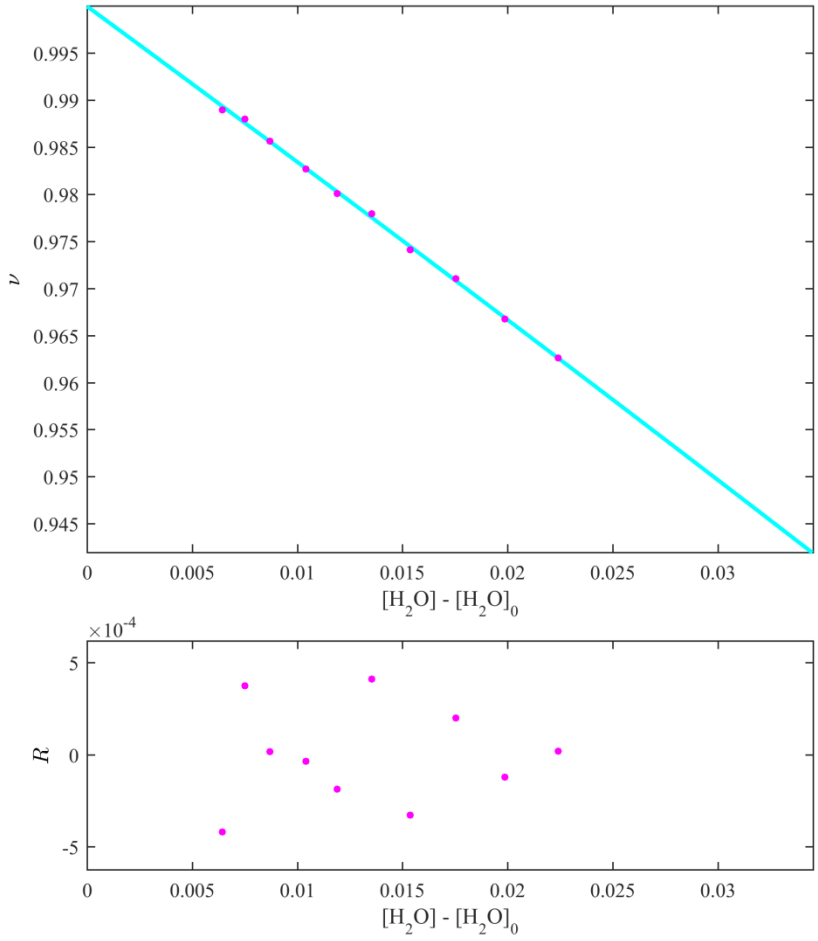

Figure S10. The empirical water correction factor (upper panel) plotted as a function of baseline corrected water mole fraction (magenta dots) for the pMGGA. The cyan line is a second order polynomial fit to the data, given by Eq. (2). ν is $[X]_0$ divided by $[X]_0^{dry}$, measured by the instrument. Corresponding residuals are given (lower panel) as magenta dots.

S3 Calibration factors

In order to calculate G for each instrument, interpolated values of $[X]_0{}^{dry}{}_{low}$ and $[X]_0{}^{dry}{}_{high}$ were generated to match measured values of $[X]_0{}^{dry}{}_{low}$ and $[X]_0{}^{dry}{}_{high}$, using a piecewise cubic hermite interpolating polynomial on Matrix Laboratory (MATLAB) R2016a. Each interpolated value of $[X]_0{}^{dry}{}_{low}$ and $[X]_0{}^{dry}{}_{high}$ was generated using measured values 4 minutes before and after the point of interpolation. These interpolated and measured $[X]_0{}^{dry}{}_{low}$ and $[X]_0{}^{dry}{}_{high}$ values are given in Figure S11 and Figure S12 for the MGGA and pMGGA, respectively. The difference between $[X]_0{}^{dry}{}_{low}$ and $[X]_0{}^{dry}{}_{high}$ at each measurement point was used to calculate individual gain factors using Eq. (6). The gain factors were then used to calculate individual offsets using Eq. (7) and Eq. (8). All individual gain factors and offsets are plotted in are given in Figure S11 and Figure S12 for the MGGA and pMGGA, respectively.

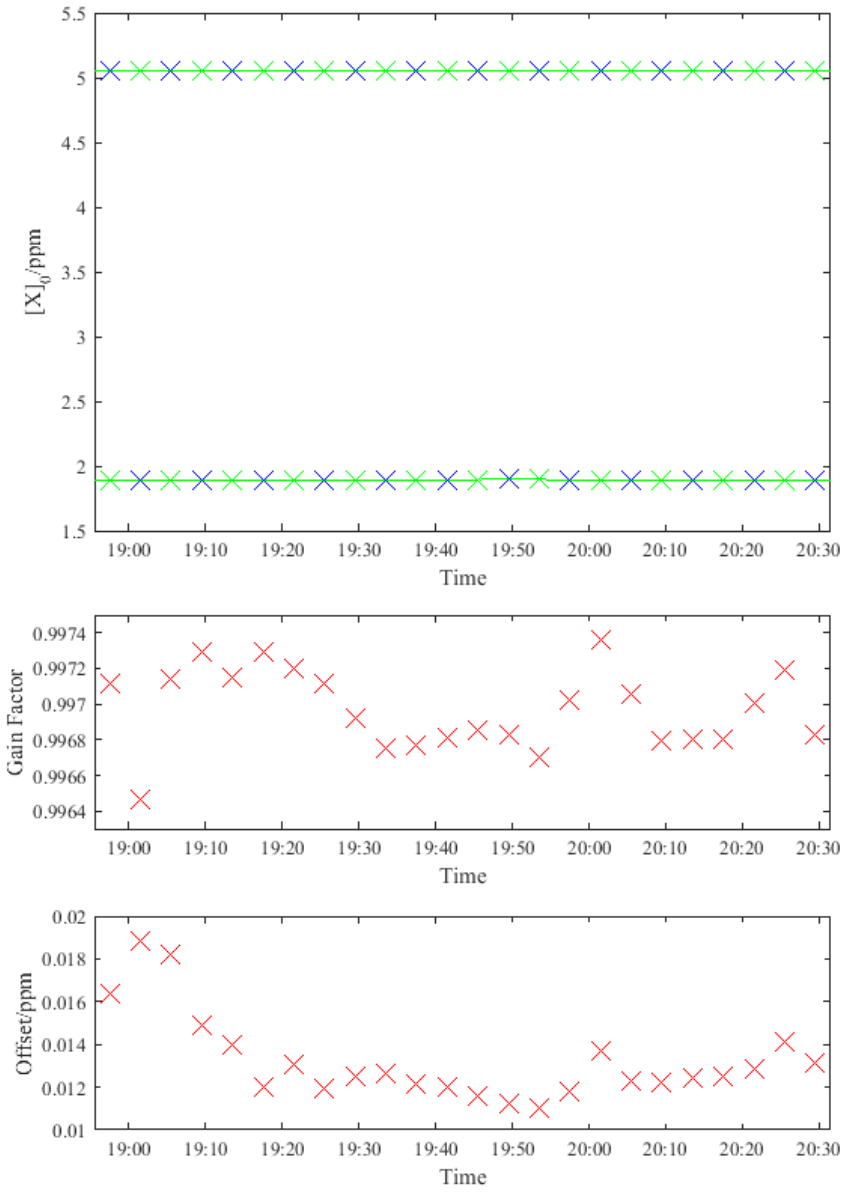

Figure S11. Measured $[X]_0^{dry}{}_{low}$ and $[X]_0^{dry}{}_{high}$ values (upper panel) as blue crosses and interpolated $[X]_0^{dry}{}_{low}$ and $[X]_0^{dry}{}_{high}$ values as green crosses for the MGGA. The interpolation curves (green line) are also given. The middle panel shows corresponding individual gain factors and the lower panel shows corresponding offsets.

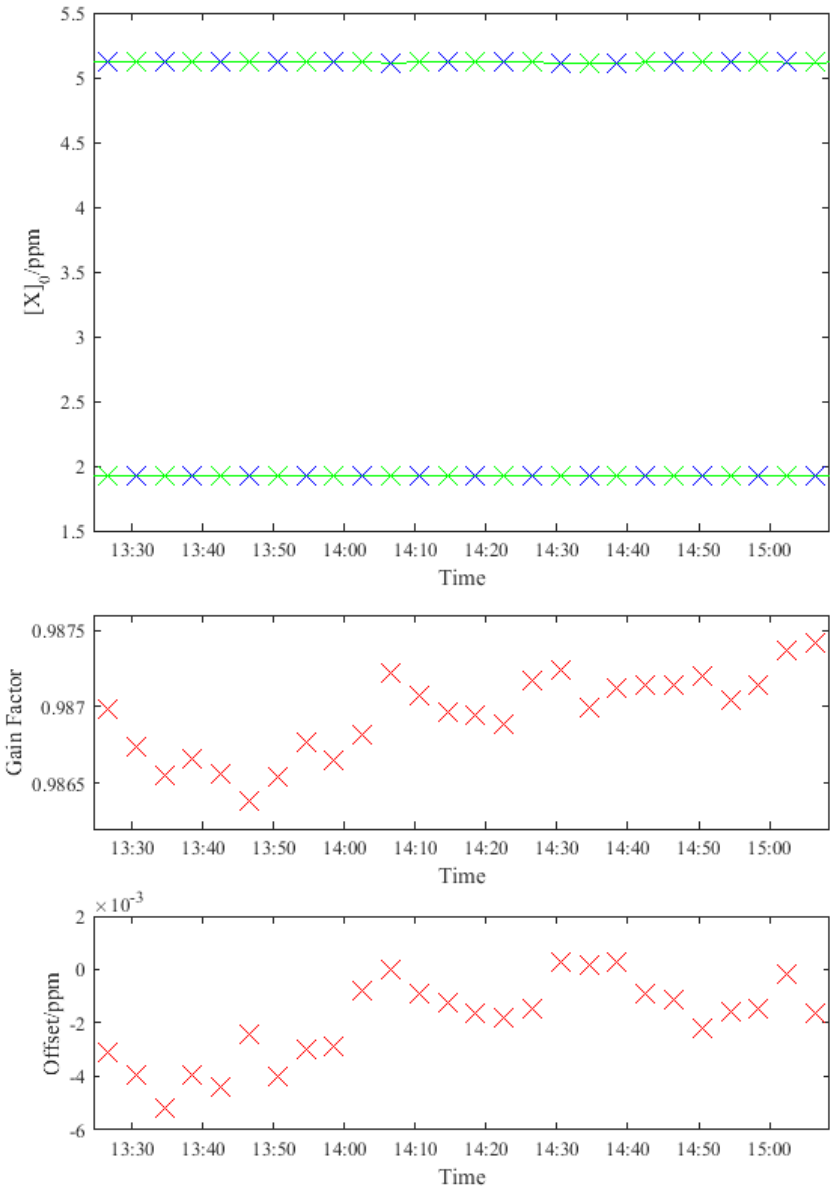

Figure S12. Measured $[X]_0^{dry}{}_{low}$ and $[X]_0^{dry}{}_{high}$ values (upper panel) as blue crosses and interpolated $[X]_0^{dry}{}_{low}$ and $[X]_0^{dry}{}_{high}$ values as green crosses for the pMGGA. The interpolation curves (green line) are also given. The middle panel shows corresponding individual gain factors and the lower panel shows corresponding offsets.

To assess the effect of variability of cell temperature and cell pressure on the gain factor, sensitivity tests were performed on the MGGA by sampling $[X]_{low}$ and $[X]_{high}$. Each standard was sampled three times for four minutes. One-minute averages from each 4-minute sampling period were taken. The mean of all three $[X]_{low}$ averages and the mean of all three $[X]_{high}$ averages were then used to derive a single test gain factor. This test was conducted at a cell pressure setting of (968.7±0.3) mbar and a cell temperature setting of (32.22±0.04)° C, which releveled a gain factor of 0.9967, in close agreement with the 0.9970±0.00023 *G* value presented in Table 3. This test was also conducted at a cell temperature setting of (44.08±0.02)° C and a pressure setting of (1025.1±0.3) mbar, which releveled a gain factor of 0.9979, in close agreement with the 0.9970±0.00023 *G* value presented in Table 3.

S4 Linearity

Linearity in the instrumental response was tested by sampling five WMO-X2004A gas standards (1.698 ppm, 1.901 ppm, 3.401 ppm, 5.031 ppm and 5.049 ppm). Over a 25-minute period, a 2-minute period of stable sampling was acquired from each standard. This sampling procedure was repeated three times, so each standard was sampled three times. A water trap was used throughout this test. Each $[X]_0^{dry}$ average was converted into $[X]$ using Eq. (1), where v was assumed to be 1 as the sampled gas was dry. Measured $[X]$ was plotted against certified $[X]$ (see Figure S13) and a linear fit was derived for the data, with a gain factor of 1.0004 and an offset of -0.00720 ppm. A third order polynomial fit was then derived for the data, with a third order coefficient of -0.000431 ppm^{-2}, a second order coefficient of 0.00633 ppm^{-1}, a first order coefficient of 0.973 and an intercept of 0.0244 ppm. Non-linearity residuals (R_L) were then derived between the linear and polynomial fit at 0.001 ppm intervals between the highest and lowest standard (see Figure S13). A polynomial was used here to apply an equal weighting across the sampled mole fraction range. σ_L could then be derived using Eq. (A), where N_L is the total number of non-linearity residuals.

$$\text{(A)} \qquad \sigma_L = \left(\frac{\Sigma({R_L}^2)}{N_L}\right)^{\frac{1}{2}}$$

σ_L was found to be ±2.3010 ppb. This uncertainty is valid across the sampled range, up to 5 ppm (the maximum mole fraction sampled during calibrations). WMO-X2004A standards are not available above this level.

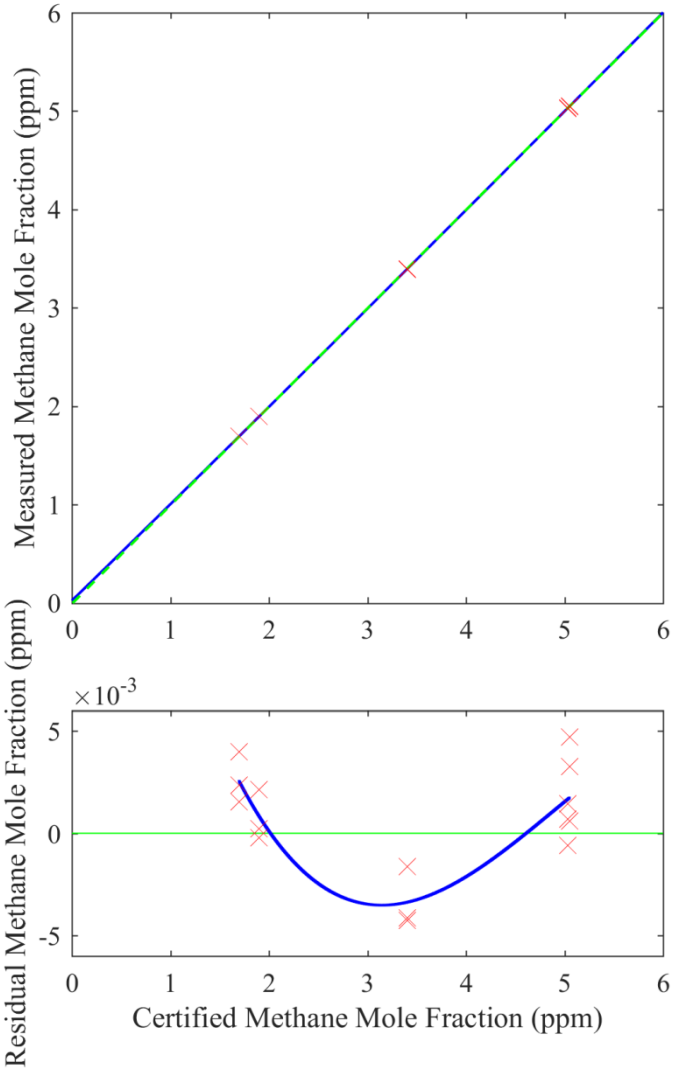

Figure S13. A linear fit (solid green line) and a third order polynomial fit (dashed blue line) applied to measured mole fraction averages (red crosses) in the MGGA against certified mole fraction (top panel). Individual measured mole fraction residuals (red crosses) are shown in the lower panel from the linear fit (solid green line), with evenly spaced 0.001 ppm residuals from the polynomial fit (blue dots) also shown.

S5 Flight survey details

The duration of each flight survey, during which $[X]_0$ measurements were used, are given in Table S1 and Table S2, for UAV1 and UAV2, respectively. Sampling periods in which there were kinks have been omitted from Table S1 for UAV1. The weighted average parallel distance (x_0) is also given. This represents the parallel distance of the sampling plane from the source, weighted to the position of enhancements in E across the sampling plane (see Shah *et al.* (2019)). The average spatial velocity of each UAV is also given in Table S1 and Table S2 which represents the velocity of the UAV as it travels across the sampling plane for the duration of $[X]_0$ measurement acquisition.

Flight survey (colour in Figure S14)	**Date**	**Controlled release number (position on Figure 3)**	**Start time**	**End time**	**Duration (s)**	**Full duration (s)**	**Spatial velocity (m s^{-1})**	**x_0 (m)**	**$\overline{u(3.3)}$ (m s^{-1})**	**$\overline{v(3.3)}$ (m s^{-1})**
T1.1 (red)	21.8. 2018	C.3 (A)	15:31:45	15:34:15	150	456	1.47	50.8	+3.4 ±0.7	+0.4 ±0.6
			15:35:35	15:35:43	9					
			15:36:35	15:37:53	78					
			15:42:48	15:45:02	134					
			15:46:35	15:48:00	85					
T1.2 (red)	23.8. 2018	C.8 (C)	11:21:02	11:26:26	324	619	1.41	48.0	+4.8 ±0.6	+1.8 ±0.9
			11:31:39	11:36:34	295					
T1.3 (green)	23.8. 2018	C.9 (C)	13:08:17	13:11:11	174	480	1.47	48.6	+5.9 ±0.7	+3.7 ±0.9
			13:12:05	13:13:04	59					
			13:18:21	13:22:29	248					
T1.4 (red)	3.9. 2018	C.10 (D)	14:05:05	14:09:58	293	435	1.46	49.9	+4.7 ±1.0	-2.5 ±1.1
			14:15:27	14:17:18	111					
			14:18:50	14:19:06	17					
			14:20:14	14:20:28	14					
T1.5 (green)	3.9. 2018	C.11 (D)	15:05:17	15:06:40	83	577	1.57	50.4	+3.7 ±0.6	-3.5 ±0.7
			15:07:47	15:11:11	204					
			15:19:22	15:24:12	290					
T1.6 (blue)	3.9. 2018	C.12 (D)	16:10:31	16:15:31	300	541	1.50	49.2	+3.6 ±0.7	-1.9 ±0.6
			16:25:42	16:27:25	103					
			16:29:48	16:32:06	138					
T1.7 (red)	4.9. 2018	C.13 (E)	11:52:16	11:57:10	294	522	1.64	49.3	-0.3 ±0.7	-2.6 ±0.5
			12:05:43	12:09:31	228					

Table S1: UAV1 flight survey details during method testing. Periods of kinking of the tubing have been isolated. The position of the controlled release corresponding to each flight survey is given in brackets after the controlled release number.

Flight survey (colour in Figure S15)	Date	Controlled release number (position on Figure 3)	Start time	End time	Full duration (s)	UAV1 *P* value used from Table S4	Spatial velocity (m s^{-1})	x_0 (m)	$\overline{u(3.3)}$ (m s^{-1})	$\overline{v(3.3)}$ (m s^{-1})
T2.1 (red)	21.8. 2018	C.1 (A)	13:22:35	13:30:00	445	T1.3	3.32	104.0	+3.4 ±1.1	+0.5 ±1.0
T2.2 (green)	21.8. 2018	C.2 (A)	14:01:17	14:09:06	469	T1.3	2.76	101.6	+3.2 ±0.7	+1.0 ±0.6
T2.3 (blue)	21.8. 2018	C.2 (A)	14:17:15	14:24:52	457	T1.3	3.77	109.6	+3.3 ±0.9	-0.1 ±0.8
T2.4 (cyan)	21.8. 2018	C.3 (A)	15:29:54	15:38:24	510	T1.3	3.56	96.9	+3.7 ±0.6	+0.6 ±0.8
T2.5 (magenta)	21.8. 2018	C.3 (A)	15:43:57	15:52:59	542	T1.3	2.98	99.3	+3.4 ±0.7	+0.3 ±0.5
T2.6 (red)	22.8. 2018	C.4 (B)	10:01:24	10:09:22	478	T1.5	2.27	57.9	+2.4 ±1.0	+3.9 ±0.7
T2.7 (green)	22.8. 2018	C.5 (B)	10:31:18	10:38:25	427	T1.5	2.53	63.7	+3.7 ±0.9	+3.7 ±1.3
T2.8 (blue)	22.8. 2018	C.6 (B)	11:28:09	11:35:44	456	T1.5	1.28	113.7	+4.3 ±0.7	+4.2 ±1.7
T2.9 (cyan)	22.8. 2018	C.7 (B)	12:30:33	12:41:04	631	T1.5	1.75	86.7	+5.2 ±1.2	+4.6 ±1.1
T2.10 (red)	23.8. 2018	C.8 (C)	10:40:15	10:47:15	420	T1.4	2.57	97.4	+5.2 ±1.3	+1.9 ±0.8
T2.11 (green)	23.8. 2018	C.8 (C)	10:55:04	11:01:38	394	T1.4	2.70	95.0	+4.4 ±1.3	+1.6 ±0.6
T2.12 (blue)	23.8. 2018	C.8 (C)	11:09:11	11:17:22	491	T1.4	2.42	95.3	+4.8 ±0.9	+1.7 ±0.6
T2.13 (cyan)	23.8. 2018	C.8 (C)	11:39:40	11:46:31	411	T1.4	3.22	75.3	+4.9 ±0.8	+0.9 ±0.3
T2.14 (magenta)	23.8. 2018	C.8 (C)	11:54:35	12:01:45	430	T1.4	2.61	68.6	+5.5 ±0.9	+2.4 ±1.6
T2.15 (yellow)	23.8. 2018	C.9 (C)	13:04:40	13:11:42	423	T1.5	3.03	101.0	+5.6 ±0.8	+4.2 ±0.8

Table S2: UAV2 flight survey details during method testing. The position of the controlled release corresponding to each flight survey is given in brackets after the controlled release number. *P* from a UAV1 flight survey with similar wind conditions is given.

S6 Controlled release details and corresponding UAV aerial flight tracks

CP grade methane (> 99.5% purity; BOC Special Products) was released from either a 10 dm^3 or 50 dm^3 steel cylinder filled to approximately 0.200 mbar. A single stage chromium-plated brass regulator with a stainless steel diaphragm (C106X/1B, BOC Special Products, BOC Ltd.) was used to control the line pressure and a mass flow controller (MCR-100SLPM-D, Alicat Scientific, Inc) was used to control the release rate. Perfluoroalkoxy alkane tubing (6.35 mm outer diameter), with a length of 15.24 m, was used to connect the regulator to the mass flow controller and 30.48 m of the same tubing was used to connect the mass flow controller to the release point. The end of this tubing was placed at the bottom of a bucket filled with stones. This ensured that the methane was released at ambient atmospheric temperature.

The date, time and location of each controlled release is given in Table S3, along with F_0. Methane was released on five days; on each day it was released from a fixed position (positions A, B, C, D and E). The position of each release location is given in Figure 3. Each UAV flight track from each controlled release location is given in Figure S14 for UAV1 and Figure S15 for UAV2.

Controlled release	**Date**	**Start time**	**End Time**	**Longitude (° E)**	**Latitude (° N)**	**Position on Figure 3**	**F_0 (g s^{-1})**
C.1	21.8.2018	12:51:00	13:30:00	-2.947005	53.788030	A	0.657
C.2		13:57:00	14:27:00				0.657
C.3		15:26:00	15:57:00				0.657
C.4	22.8.2018	09:57:00	10:25:00	-2.946540	53.787610	B	0.657
C.5		10:30:00	10:40:00				0.657
C.6		11:05:00	11:41:00				0.657
C.7		12:25:00	13:00:00				0.657
C.8	23.8.2018	10:35:00	12:42:00	-2.946855	53.787730	C	1.095
C.9		13:00:00	13:25:00				0.657
C.10	3.9.2018	13:58:00	14:25:00	-2.944920	53.787993	D	0.657
C.11		14:57:00	15:40:00				0.657
C.12		16:03:00	16:34:00				0.657
C.13	4.9.2018	11:44:00	12:13:00	-2.944524	53.788288	E	0.657

Table S3: The duration of controlled methane release from one of five locations, plotted in Figure 3.

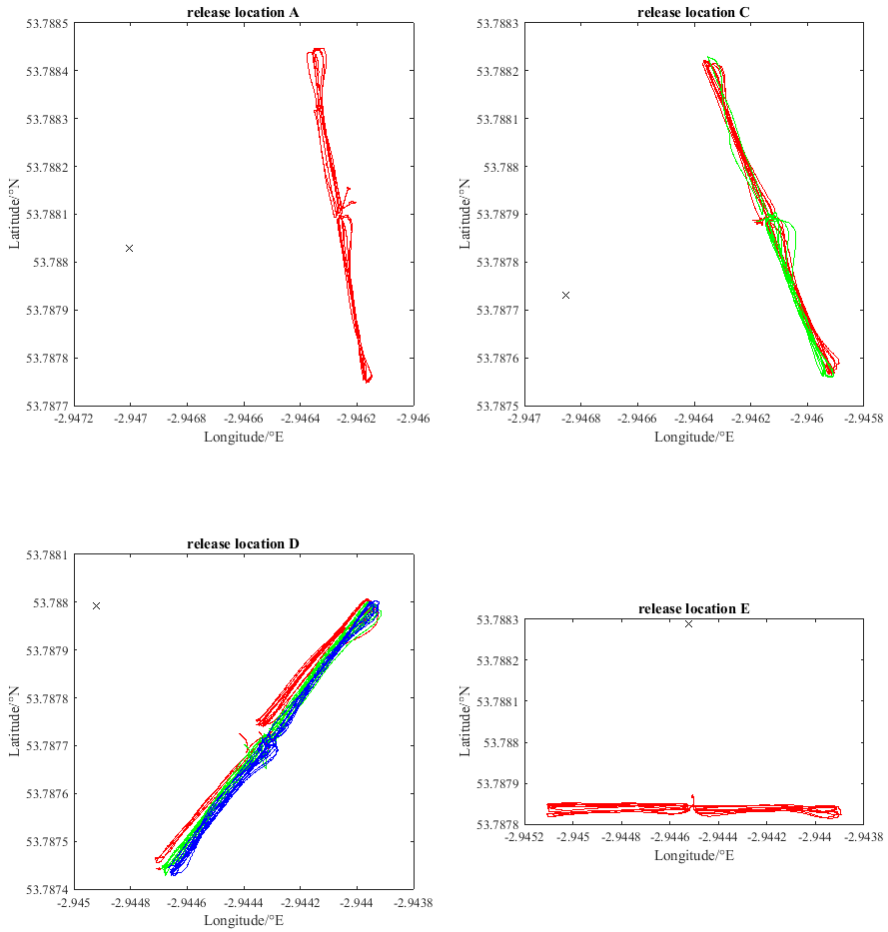

Figure S14. Aerial plots of UAV1 flight tracks (coloured dots), according to each controlled release location (black cross). The colour of each flight track is given in Table S1 and the release location labels are assigned in Table S3.

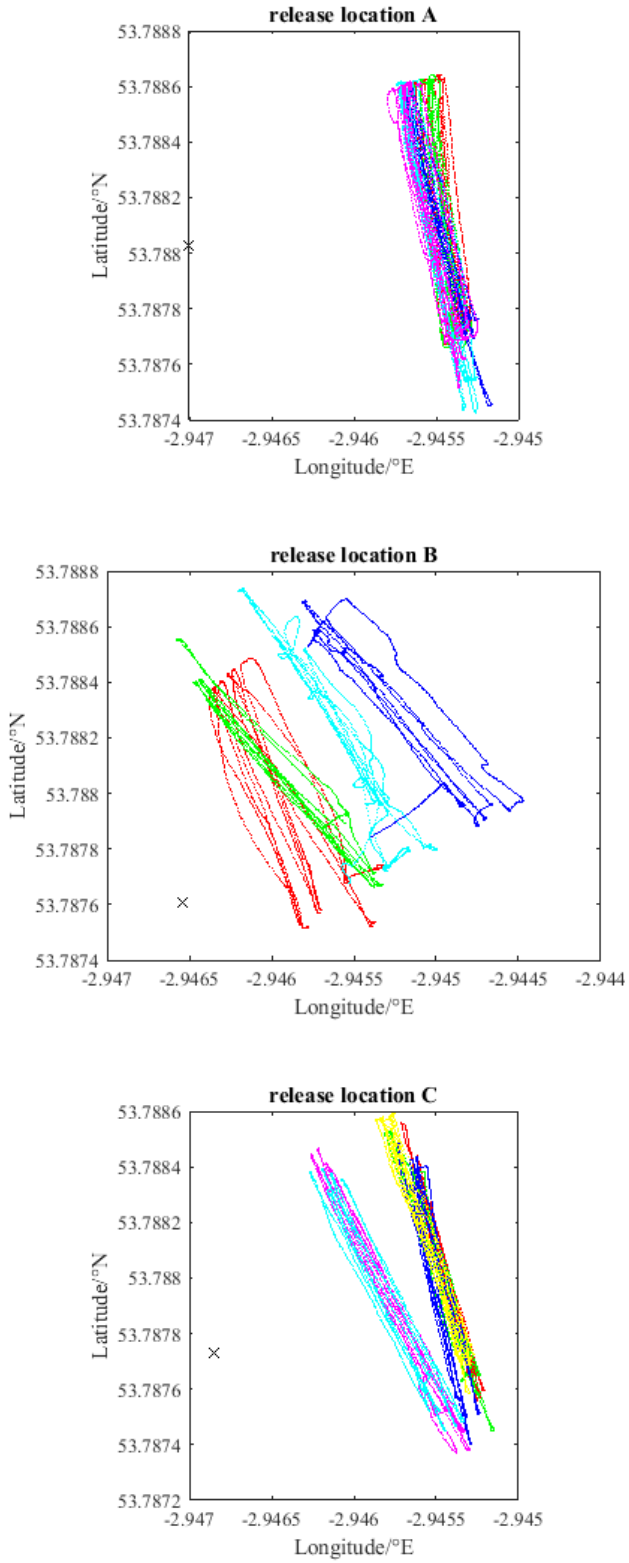

Figure S15. Aerial plots of UAV2 flight tracks (coloured dots), according to each controlled release location (black cross). The colour of each flight track is given in Table S2.

S7 Wind profiles and uncertainties

A wind sensor was mounted on-board UAV1 to characterise the change in winds with height. During the flight surveys, it was observed that the wind field was distorted in the plane parallel to UAV travel. Therefore the wind component perpendicular to the orientation of the sampling plane as a function z ($WS^{UAV}(z)$) was derived. The wind sensor was mounted on a pole on top of the UAV, 305 mm above the plane of the propellers, to minimise the influence of the propellers on the wind field. CFD modelling shows that air in funnelled in towards the propellers from the sides rather than from above (Zhou *et al.*, 2018). Furthermore, the UAV was rotated by 180° at the end of each transect to cancel out any distortion of the wind field that may otherwise occur. This means to say that if there was a wind vector offset in the wind sensor due to the rotation of the propellers, the same offset would be present in the return transect, thus cancelling out this potential small wind vector over many transects.

$WS^{UAV}(z)$ was fitted using Eq. (B) for the full duration of each UAV1 flight survey. $WS^{UAV}(3.3)$ is $WS^{UAV}(z)$ derived at 3.3 m and P is the wind power (see Table S4 for values).

(B) $$WS^{UAV}(z) = WS^{UAV}(3.3) \cdot \left(\frac{z}{3.3}\right)^{P}$$

Each "j" wind residual (WR), between measured $WS^{UAV}(z)$ values and those predicted by Eq. (B), were used to derive the UAV wind uncertainty (ΔWS^{UAV}), using Eq. (C).

(C) $$\Delta WS^{UAV} = \left(\frac{\sum_{j=1}^{N}(WR_j^{\,2})}{NWR}\right)^{\frac{1}{2}}$$

Wind profiles of $WS^{UAV}(z)$ along with ΔWS^{UAV} during method testing are given in Figure S16.

Flight survey	***P***	$\boldsymbol{WS^{UAV}(3.3)}$ **(m s^{-1})**
T1.1	0.090	4.5
T1.2	0.127	5.5
T1.3	0.104	7.7
T1.4	0.213	6.2
T1.5	0.190	5.7
T1.6	0.052	6.4
T1.7	0.222	3.0

Table S4: Coefficients used to fit the wind profiles in Figure S16 to Eq. (B) for each UAV1 flight survey during method testing.

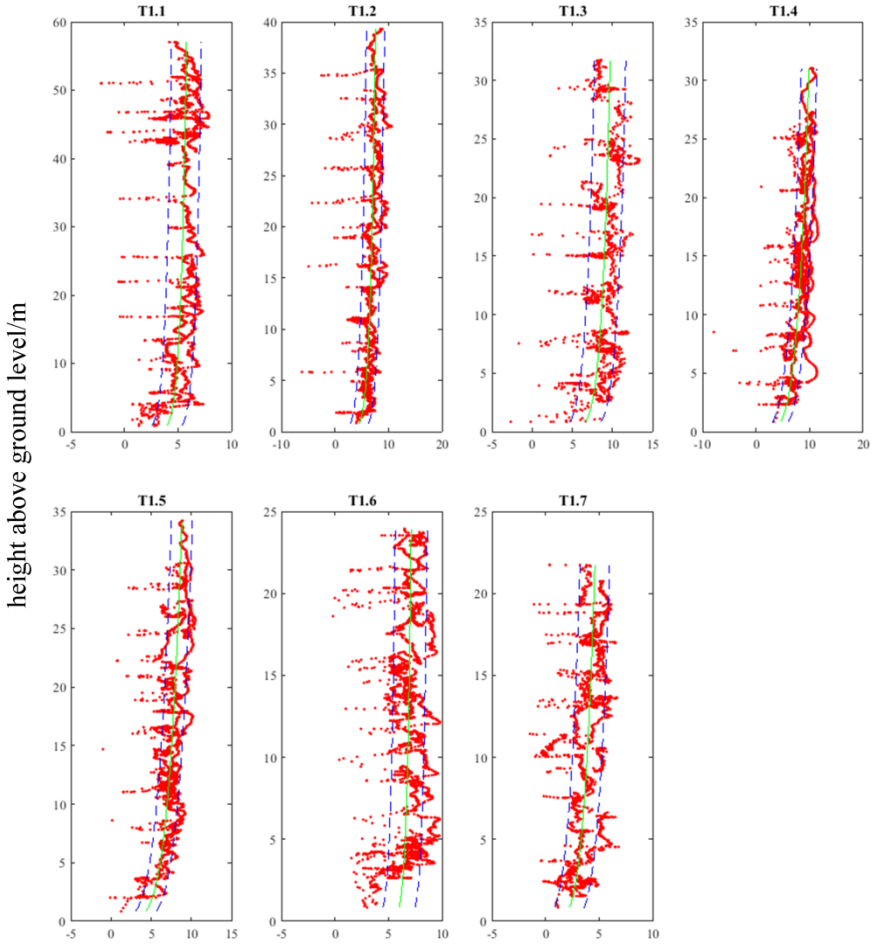

Figure S16. The wind speed component perpendicular to the orientation of the sampling plane, derived from the anemometer mounted on UAV1 (red dots) for each UAV1 method testing flight survey. $WS^{UAV}(z)$ given by Eq. (B) is also plotted (solid green lines), along with corresponding ΔWS^{UAV} bounds from Eq. (C) (dashed blue lines).

In order to derive a reliable wind speed profile with height, $WS^{UAV}(z)$ measurements were compared to a stationary anemometer on the ground. This cross-referencing approach means that the accuracy of the on-board wind sensor was not important, provided that it had a linear wind speed response. The linear response of the on-board wind sensor was tested by plotting $WS^{UAV}(z)$ against the wind component perpendicular to the orientation of the sampling plane from the stationary anemometer at 3.3 m, for the full duration of UAV sampling in Figure S16. A linear fit with a gradient of 1.19 was derived, with all points agreeing with the fit, within uncertainty, thus confirming the wind sensor's suitability to derive $WS^{UAV}(z)$ on-board UAV1, due to its linear response.

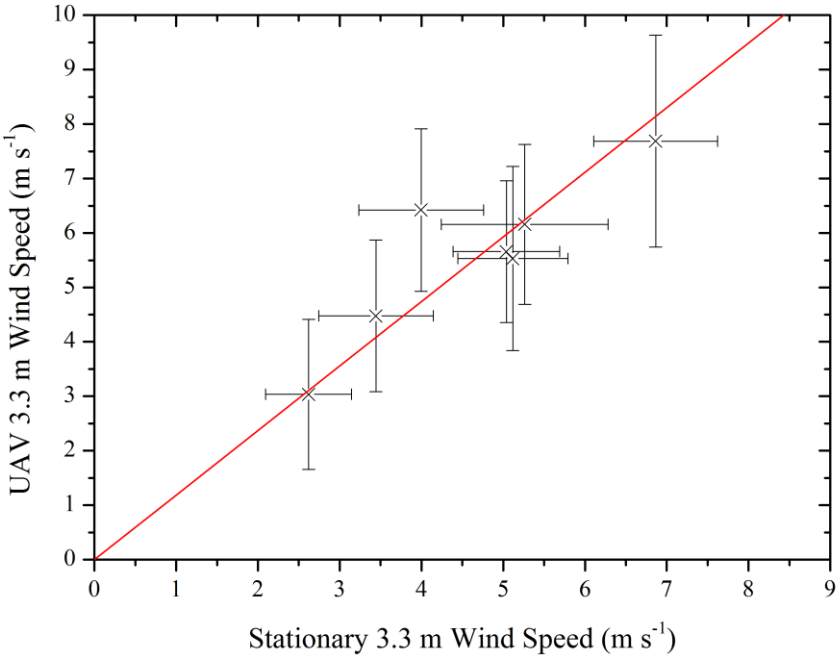

Figure S17. The wind component perpendicular to the orientation of the sampling plane from the stationary anemometer plotted against $WS^{UAV}(3.3)$ (black crosses) with a linear fit for the data, forced to a zero intercept, also shown (solid red line). Vertical error bars represent ΔWS^{UAV} and horizontal error bars represent uncertainty in the stationary wind speed measurement.

The average zonal wind velocity at 3.3 m ($\overline{u(3.3)}$) and the average meridional wind velocity at 3.3 m ($\overline{v(3.3)}$) were derived from measurements made by the stationary anemometer, for the full duration of each flight survey (see Table S1 and Table S2). $\overline{u(3.3)}$ and $\overline{v(3.3)}$ were then used to derive the zonal wind velocity as a function of z ($u(z)$) and meridional wind velocity as a function of z ($v(z)$) using Eq. (D) and Eq. (E), respectively, for the duration of each flight survey.

(D) $$u(z) = \overline{u(3.3)} \cdot \left(\frac{z}{3.3}\right)^{P}$$

(E) $$v(z) = \overline{v(3.3)} \cdot \left(\frac{z}{3.3}\right)^{P}$$

As $WS^{UAV}(z)$ was not measured on UAV2, a wind power was used in Eq. (D) and Eq. (E), corresponding to a flight survey by UAV1 with similar wind conditions, for all UAV2 flight surveys (see Table S2 for choice of P). $u(z)$ and $v(z)$ were combined to derive $WS(z)$ for each flight survey, using Eq. (F).

(F) $$WS(z) = \left(u(z)^2 + v(z)^2\right)^{\frac{1}{2}}$$

NWR is the total number of wind residuals. The uncertainty in $u(z)$ ($\sigma_{u(z)}$) and the uncertainty in $v(z)$ ($\sigma_{v(z)}$) were calculated using Eq. (G) and Eq. (H), respectively.

(G) $$\sigma_{u(z)} = \left(\left(\sigma_{u(3.3)} \cdot \left(\frac{z}{3.3}\right)^{P}\right)^2 + \left(\Delta WS^{UAV}\right)^2\right)^{\frac{1}{2}}$$

(H) $$\sigma_{v(z)} = \left(\left(\sigma_{v(3.3)} \cdot \left(\frac{z}{3.3}\right)^{P}\right)^2 + \left(\Delta WS^{UAV}\right)^2\right)^{\frac{1}{2}}$$

$\sigma_{u(3.3)}$ is the uncertainty in $\overline{u(3.3)}$ and $\sigma_{v(3.3)}$ is the uncertainty in $\overline{v(3.3)}$, derived from the standard deviation in individual measurements made by the stationary sonic anemometer. The uncertainty in $WS(z)$ ($\sigma_{WS(z)}$) can be derived by combining $\sigma_{u(z)}$ and $\sigma_{v(z)}$, using Eq. (I).

(I) $$\sigma_{WS(z)} = \left(\left(\frac{u(z) \cdot \sigma_{u(z)}}{WS(z)} \right)^2 + \left(\frac{v(z) \cdot \sigma_{v(z)}}{WS(z)} \right)^2 \right)^{\frac{1}{2}}$$

S8 Testing flux results

Flux results and uncertainties for each flight conducted by both UAV1 and UAV2 during the controlled methane gas release are given in Table S5.

Flight survey	F_0 (g s^{-1})	F_e (g s^{-1})	σ^- (g s^{-1})	σ^+ (g s^{-1})	σ_F (g s^{-1})
T2.1	0.657	0.27	-0.23	+0.30	±0.14
T2.2	0.657	0.30	-0.27	+0.36	±0.17
T2.3	0.657	1.55	-1.32	+1.60	±0.87
T2.4	0.657	0.49	-0.42	+0.52	±0.22
T1.1	0.657	0.21	-0.20	+0.22	±0.09
T2.5	0.657	0.84	-0.73	+0.92	±0.43
T2.6	0.657	0.66	-0.61	+0.86	±0.33
T2.7	0.657	1.04	-0.83	+1.04	±0.53
T2.8	0.657	0.55	-0.41	+0.70	±0.22
T2.9	0.657	0.76	-0.67	+1.04	±0.27
T2.10	1.095	0.96	-0.77	+0.93	±0.45
T2.11	1.095	0.95	-0.79	+1.05	±0.47
T2.12	1.095	1.25	-1.04	+1.27	±0.53
T1.2	1.095	1.36	-1.18	+1.25	±0.48
T2.13	1.095	1.48	-1.17	+1.47	±0.74
T2.14	1.095	1.40	-1.20	+1.57	±0.61
T2.15	0.657	0.72	-0.63	+0.80	±0.27
T1.3	0.657	0.76	-0.71	+0.79	±0.24
T1.4	0.657	1.03	-0.87	+0.96	±0.33
T1.5	0.657	1.37	-1.15	+1.22	±0.42
T1.6	0.657	0.74	-0.58	+0.61	±0.31
T1.7	0.657	0.34	-0.30	+0.32	±0.19

Table S5: Known emission fluxes, calculated NGI emission fluxes and NGI flux uncertainty bounds for each UAV flight survey carried out during method testing. The flights are listed in chronologically in order of take-off time.

S9 Measurement uncertainty components

The σ_F uncertainty is formed by combining individual flux density uncertainties, using Eq. (J). Each flux density uncertainty contains a wind uncertainty component and a mole fraction enhancement uncertainty component. σ_F due to wind ($\sigma_F W$) and σ_F due to mole fraction enhancement ($\sigma_F E$) can be derived using Eq. (K) and Eq. (L), respectively. This allows the importance of these individual uncertainty components to be assessed. $\sigma_F W$ and $\sigma_F E$ for each flight survey are given in Table S6, as a fraction of σ_F. On average, $\sigma_F W$ was ±90%±8% of σ_F and $\sigma_F E$ was ±37%±21% of σ_F.

(J) $$\sigma_F = F_e \cdot \left(\frac{\Sigma\left(q^2 \cdot \left(\left(\frac{\sigma_{WS(z)}}{WS(z)} \right)^2 + \left(\frac{\sigma_E}{E} \right)^2 \right) \right)}{\Sigma(q^2)} \right)^{\frac{1}{2}}$$

(K) $$\sigma_F W = F_e \cdot \left(\frac{\Sigma\left(q^2 \cdot \left(\frac{\sigma_{WS(z)}}{WS(z)} \right)^2 \right)}{\Sigma(q^2)} \right)^{\frac{1}{2}}$$

(L) $$\sigma_F E = F_e \cdot \left(\frac{\Sigma\left(q^2 \cdot \left(\frac{\sigma_E}{E} \right)^2 \right)}{\Sigma(q^2)} \right)^{\frac{1}{2}}$$

σ_E measurements from each flight survey could be converted into average σ_E expressed as a dry mole fraction ($\sigma_E D$) using Eq. (M). The $\sigma_E D$ average for sampling from each flight survey is given in Table S7.

(M) $$\sigma_E D = \frac{\sigma_E}{\rho \cdot M}$$

Flight survey	σ_F **(g s^{-1})**	$\sigma_F W/\sigma_F$	$\sigma_F E/\sigma_F$
T2.1	±0.14	0.932	0.362
T2.2	±0.17	0.794	0.607
T2.3	±0.87	0.897	0.442
T2.4	±0.22	0.889	0.458
T1.1	±0.09	0.998	0.063
T2.5	±0.43	0.849	0.528
T2.6	±0.33	0.900	0.437
T2.7	±0.53	0.851	0.525
T2.8	±0.22	0.950	0.311
T2.9	±0.27	0.929	0.370
T2.10	±0.45	0.819	0.574
T2.11	±0.47	0.915	0.404
T2.12	±0.53	0.847	0.531
T1.2	±0.48	0.999	0.034
T2.13	±0.74	0.746	0.531
T2.14	±0.61	0.783	0.622
T2.15	±0.27	0.792	0.611
T1.3	±0.24	0.955	0.297
T1.4	±0.33	0.979	0.202
T1.5	±0.42	0.999	0.054
T1.6	±0.31	0.999	0.049
T1.7	±0.19	0.999	0.040

Table S6: Measurement flux uncertainties due to uncertainties in mole fraction enhancements and wind speed alone, as a fraction of measurement flux uncertainty, also given. The flights are listed in chronologically in order of take-off time.

Flight survey	$\sigma_E D$ average (ppm)
T2.1	±30.5423±0.0007
T2.2	±58.4126±0.0003
T2.3	±65.5064±0.0018
T2.4	±31.8550±0.0005
T1.1	±26.7440±0.0598
T2.5	±46.6196±0.0006
T2.6	±55.5994±0.0007
T2.7	±106.4894±0.0006
T2.8	±13.2276±0.0002
T2.9	±32.9525±0.0013
T2.10	±127.0895±0.0012
T2.11	±68.4117±0.0007
T2.12	±76.5790±0.0008
T1.2	±20.3989±0.2209
T2.13	±156.9230±0.0007
T2.14	±177.3322±0.0016
T2.15	±35.3231±0.0003
T1.3	±14.2354±0.0018
T1.4	±22.5793±0.0390
T1.5	±8.4427±0.0570
T1.6	±22.7424±0.0515
T1.7	±21.0254±0.0818

Table S7: The average mole fraction enhancement uncertainty and corresponding standard deviation for each UAV flight survey carried out during method testing. The flights are listed in chronologically in order of take-off time.

305

S10 Cell temperature and cell pressure during sampling

Cell temperature and cell pressure were recorded for each UAV flight survey. The average and standard deviation cell pressure and cell temperature for UAV1 and UAV2 are given in Figure S18 and Figure S19, respectively. The average and standard deviation cell pressure and cell temperature during calibrations for each instrument used during UAV sampling is also given in Figure S18 and Figure S19.

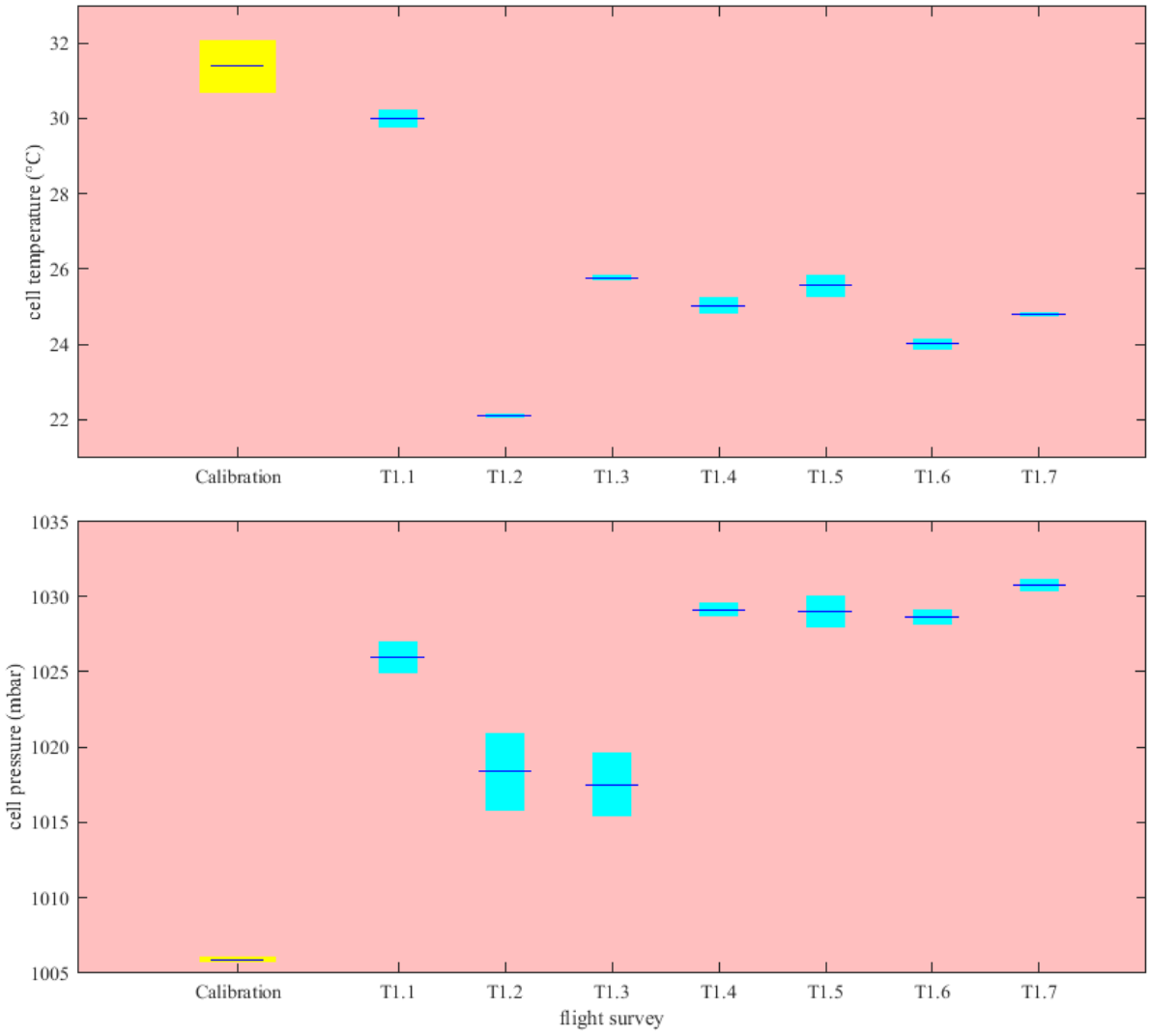

Figure S18. Average cell temperature and pressure cell (horizontal blue lines) over standard deviation variability (vertical cyan bars) for each UAV1 flight survey, measured by the MGGA. The average cell temperature and cell pressure (horizontal blue lines) over the standard deviation variability (vertical yellow bar) for the MGGA calibration is also given.

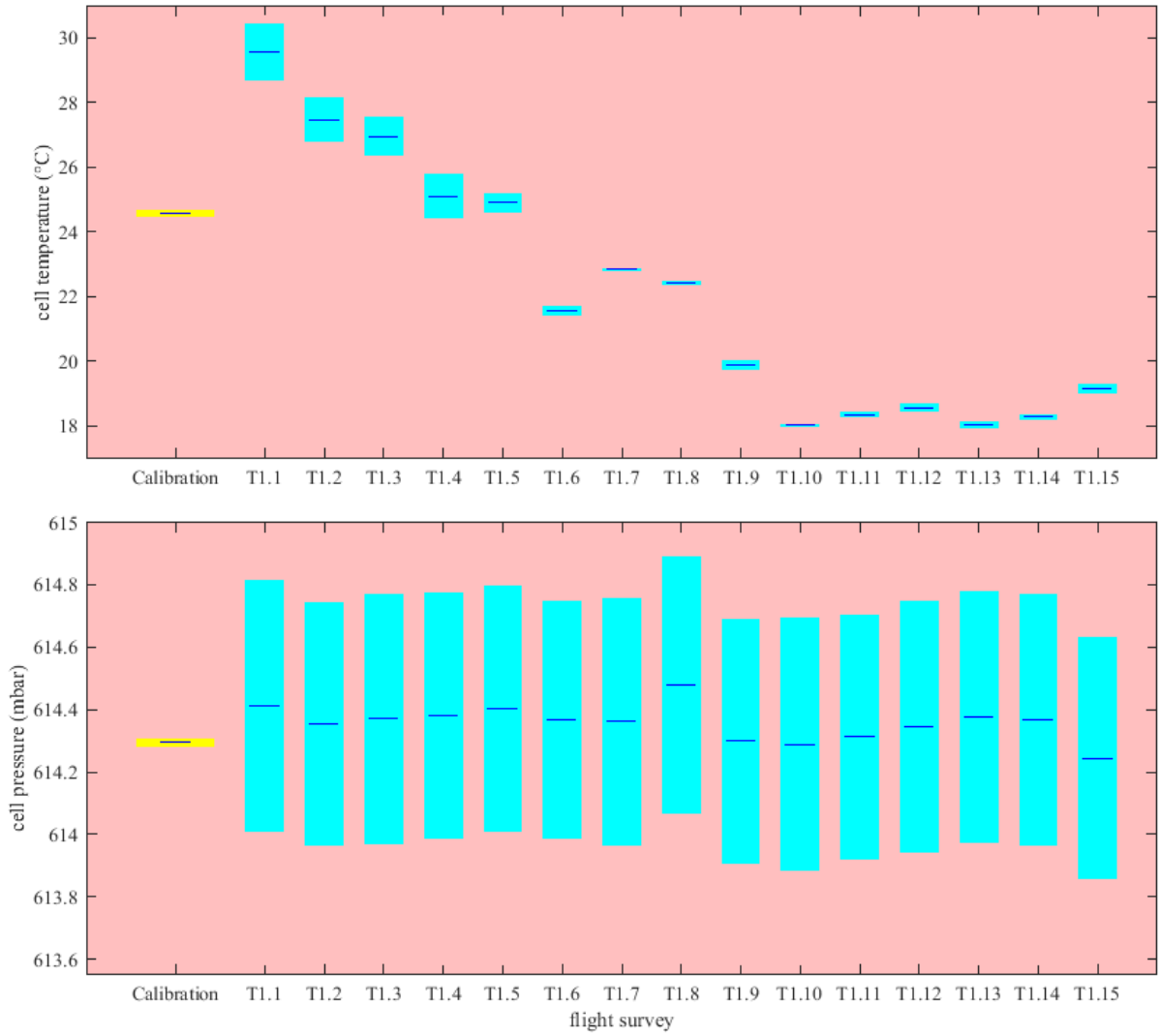

Figure S19. Average cell temperature and pressure cell (horizontal blue lines) over standard deviation variability (vertical cyan bars) for each UAV2 flight survey, measured by the pMGGA. The average cell temperature and cell pressure (horizontal blue lines) over the standard deviation variability (vertical yellow bar) for the pMGGA calibration is also given.